Energy &
Environmental Materials WILEY

Manipulating the Macroscopic and Microscopic Morphology of Large-Area Gravure-Printed ZnO Films for High-Performance Flexible Organic Solar Cells

Zhenguo Wang, Jingbo Guo, Yaqin Pan, Jin Fang, Chao Gong, Lixin Mo, Qun Luo* , Jian Lin*, and Changqi Ma*

Gravure printing is a promising large-scale fabrication method for flexible organic solar cells (FOSCs) because it is compatible with two-dimension patternable roll-to-roll fabrication. However, the unsuitable rheological property of ZnO nanoinks resulted in unevenness and looseness of the gravure-printed ZnO interfacial layer. Here we propose a strategy to manipulate the macroscopic and microscopic of the gravure-printed ZnO films through using mixed solvent and poly(vinylpyrrolidone) (PVP) additive. The regulation of drying speed effectively manipulates the droplets fusion and leveling process and eliminates the printing ribbing structure in the macroscopic morphology. The additive of PVP effectively regulates the rheological property and improves the microscopic compactness of the films. Following this method, large-area ZnO:PVP films (28×9 cm^2) with excellent uniformity, compactness, conductivity, and bending durability were fabricated. The power conversion efficiencies of FOSCs with gravure-printed AgNWs and ZnO:PVP films reached 14.34% and 17.07% for the 1 cm^2 PM6:Y6 and PM6:L8-BO flexible devices. The efficiency of 17.07% is the highest value to date for the 1 cm^2 FOSCs. The use of mixed solvent and PVP addition also significantly enlarged the printing window of ZnO ink, ensuring high-quality printed thin films with thicknesses varying from 30 to 100 nm.

Z. Wang, Dr. Q. Luo, Dr. J. Lin, Prof. C. Ma
School of Nano-Tech and Nano-Bionics, University of Science and Technology of China, Hefei 230026, China
E-mail: qluo2011@sinano.ac.cn
E-mail: jlin2010@sinano.ac.cn
E-mail: cqma2011@sinano.ac.cn
Z. Wang, J. Guo, Y. Pan, Dr. J. Fang, C. Gong, Dr. Q. Luo, Dr. J. Lin, Prof. C. Ma
i-Lab & Printable Electronics Research Center, Suzhou Institute of Nano-Tech and Nano-Bionics, Chinese Academy of Sciences (CAS), Suzhou 215123, China
Y. Pan, Dr. L. Mo
Beijing Engineering Research Center of Printed Electronics, Beijing Institute of Graphic Communication, Beijing 102600, China
C. Gong, Dr. J. Lin, Prof. C. Ma
Jiangxi Institute of Nanotechnology, Chinese Academy of Sciences (CAS), Nanchang 330200, China
The ORCID identification number(s) for the author(s) of this article can be found under https://doi.org/10.1002/eem2.12592.

1. Introduction

Organic solar cells (OSCs) have received extensive attention due to their unique advantages of flexible, lightweight, nontoxic, low-cost, and large-area printing fabrication compatible.[1–6] In recent years, owing to the rapid developments of new organic semiconductors,[2,7] optimization of the active layer morphology,[8,9] and interface engineering,[10,11] the power conversion efficiency (PCE) of single-junction OSCs has exceeded 19%.[8] However, high-efficiency devices are usually fabricated by spin-coating, which is incompatible with continuous large-scale fabrication and hinders the commercialization of organic solar cells.[12–15]

At present, blade coating and slot-die coating are widely used in the laboratory to fabricate large-area OSCs due to their simple operation and low requirements on the rheological properties of the ink.[13,16–18] However, doctor-blading is not patternable, thereby laser or mechanical scribing is needed to pattern the stripe during module fabrication.[14,19] Slot-die has the function of 1D patterning and can directly fabricate strip-shaped modules, yet it can only prepare strip-shaped modules, which would seriously affect the aesthetics of the OSCs.[14,20] Gravure printing is a promising technology for large-area fabrication due to its advantages of high resolution, high speed, 2D patternable, and roll-to-roll compatibility.[21–24] The minimum gap of pattern deposited by gravure printing can be reduced as low as 100 μm, and thereby GFF of the directly printed module can reach higher than 90%.[14] In addition, the feature of 2D patternable makes it possible to achieve modules with various shapes, which would greatly improve the designability of OSCs.[22,25,26] However, compared with coating routes, gravure printing has higher requirements on rheological properties such as volatilization speed and viscosity of the inks.[14,22,23,27,28] During gravure printing, the ink is transferred from the cavities of the gravure roller to the substrate, and then the droplets undergo a process of fusion, leveling, volatilization, drying, and finally form a film.[27,29] Unexpected films with ribbing structures, uneven surfaces, poor compactness, and pinholes always form if the inks have inappropriate rheological properties.[27,28]

Zinc oxide (ZnO) is a widely used printable electron transporting layer (ETL) with the advantages of low work function, high electron

mobility, high optical transparency, and low-temperature fabrication compatibility.[11,30–34] However, the low viscosity of ZnO inks would lead to the formation of unevenness and looseness of ZnO films, especially when printing on rough surfaces. Though it is relatively easy to adjust the ink rheological properties to meet the needs of gravure printing through regulating the ink formulation,[35] it is difficult to optimize the inks formulation in the case of OSCs since slight variation in inks formulation would greatly impact the device performance.[36–38] Even the addition of a small number of additives may cause a serious decline in the optoelectronic properties of ZnO thin films.[39,40] Therefore, regulating the rheological properties of inks to improve the macroscopic and microscopic morphology is a key challenge of large-area gravure-printed ZnO films.

In this study, we proposed a strategy to regulate the printable inks and successfully printed large-area ZnO films with improved macroscopic and microscopic morphology, as well as good photoelectronic properties. By using a mixed solvent of ethanol and butanol, together with introducing polymer poly(vinylpyrrolidone) (PVP) in the ZnO ink, the rheological properties such as viscosity and volatilization speed of the ink are improved. Through this method, the macroscopic ribbing structures and microscopic uncompact issues of the printed ZnO films were solved. In addition, the use of this ink also ensured the photoelectronic properties of the printed ZnO films. As a consequence, large-area (28 × 9 cm^2) ZnO films with high uniformity, compactness, conductivity, and bending durability were printed. More importantly, large-area thin films around 30 nm with extremal homogeneity were achieved through gravure printing from the ZnO:PVP inks. The device performance of small-area flexible OSCs with PM6:Y6 active layers increased from 13.65% to 15.01%. The 1 cm^2 PM6:L8-BO flexible OSCs with gravure printed ZnO:PVP ETL gave a recorded efficiency of 17.07%.

2. Results and Discussion

2.1. Leveling Model of Gravure Printing

Figure 1a shows the schematic diagram of the high-speed gravure printing process of ZnO ETL and AgNW electrodes. The gravure roller consists of a uniform cavity structure (as shown in Figure S1, Supporting Information). Due to the uniform cavity structure of the gravure roller, gravure printing has the advantage of large-area uniformity. In addition, the gravure roller can be designed with any pattern with high resolution. The gravure printing process is mainly divided into three steps.[27,29] First, the ink is filled into the gravure cavities by the doctor, and the excess ink is removed from the nonpatterned region. Subsequently, the ink is transferred from the cavities of the gravure roller to the substrate under a specific pressure with the help of the impression roller. Then, the ink droplets merge and level on the substrate driven by its surface tension. Finally, the solvent volatilizes and inks solidify to form a film. Due to the more complex rheological behavior during gravure printing, it has higher requirements on rheological properties such as volatilization speed and viscosity for the inks.

Figure 1b shows the schematic diagram of droplet fusion, leveling, and drying processes during gravure printing. Driven by surface tension, the ink droplets would level on the substrate. Such a process is highly determined by solvent volatilization speed. When the volatilization speed is too fast, the ink droplets cannot coalesce and level well on the substrates, resulting in obvious ribbing structures in the gravure-printed film. Such a ribbing structure can be usually suppressed through tuning the inks rheological properties and the drying
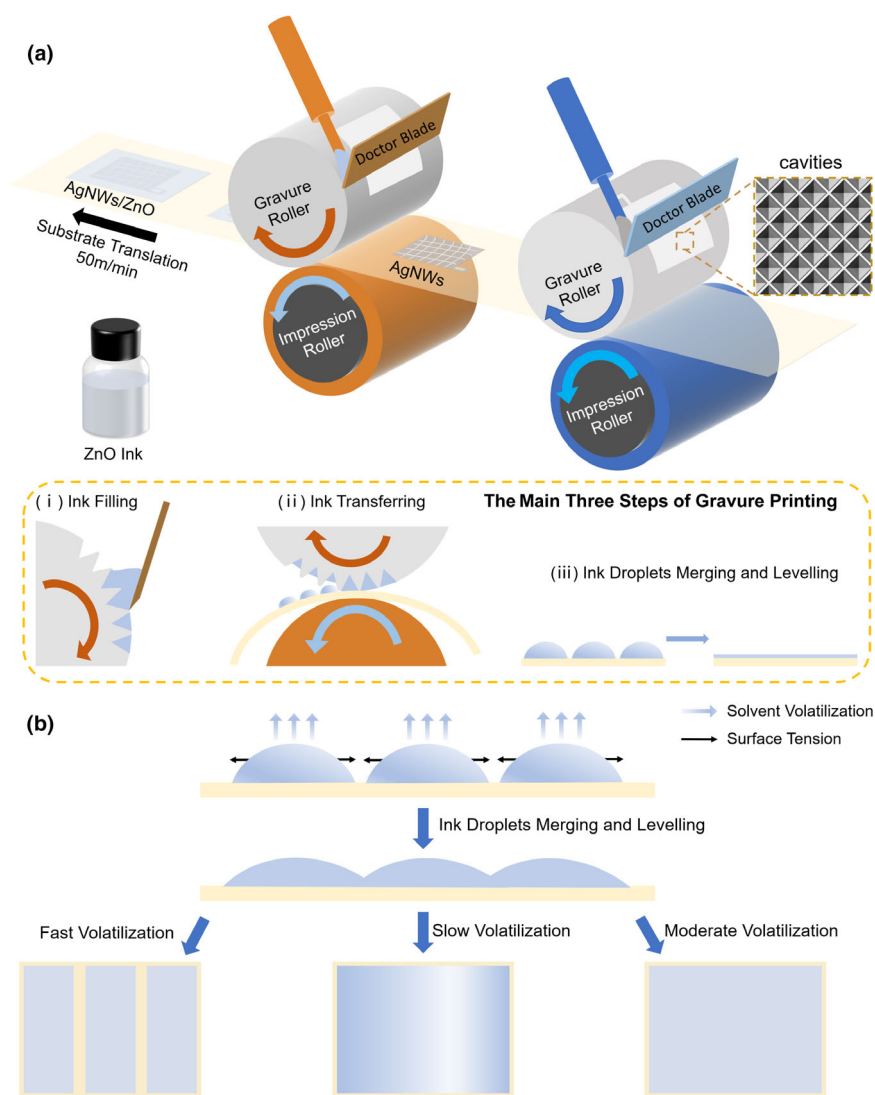

Figure 1. a) Schematic diagram of the high-speed gravure printing process of AgNWs and ZnO printing. Insets: i) the doctor blade forces the ink to fill the gravure cavities; ii) the ink is transferred from the cavities of the gravure roller to the substrate; and iii) ink droplets merging and leveling on the substrate. b) The formation mechanism of the gravure-printed ZnO and ZnO:PVP fims.
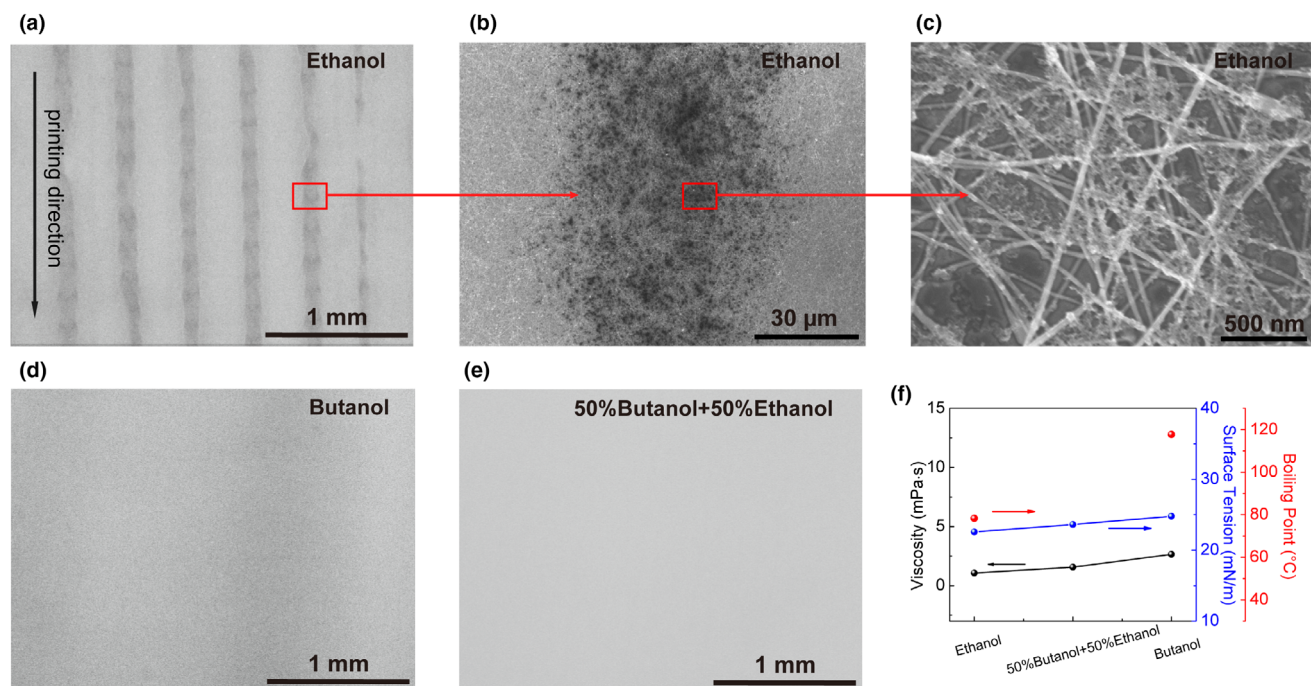
Figure 2. a–e) SEM images of the gravure-printed ZnO films from a–c) ethanol d) butanol and e) 50% butanol and 50% ethanol dispersed ZnO inks. f) Surface tension, boiling point, and viscosity at a shear rate 1 s^{-1} for ethanol, 50% butanol and 50% ethanol, and butanol dispersed ZnO inks.

process.[27,28] When the volatilization speed of the ink is too slow, though the droplet would effectively coalesce and level, excessive movement of the ink droplets also occurs, which causes the unevenness of the film. Only when the volatilization speed is appropriate, the droplets will have sufficient time to coalesce and level on the substrate and do not uncontrollably move during the high-speed printing process. Thus, a uniform film can be formed on the substrate.

2.2. Elimination of the Ribbing Structures in the Gravure-Printed ZnO Films Through Solvent Engineering

As shown by the schematic diagram of the inks leveling model during gravure printing (Figure 1), we know the solvent drying speed would have a deciding role in the films quality. Guided by this mechanism, we first studied the influence of solvent on the macroscopic morphology of the printed ZnO films. Ethanol with a boiling point of 78.3 °C was used to disperse ZnO nanoparticles since such kind of ink is regularly used in spin-coating. The SEM image of the gravure-printed ZnO film is shown in **Figure 2a–c**. From this image, it can be found that there are serious ribbing structures in the film. Further in the SEM image, we found poor coverage of ZnO on the top of AgNWs in the ribbing region. A large number of AgNWs were not covered by ZnO nanoparticles, which would cause leakage current or even short circuit of the device. From Figure S3, Supporting Information, it can be found that the contact angle of the ethanol-dispersed ZnO ink on the AgNW electrode is only 1.1°, indicating that the ethanol-dispersed ZnO ink has good wettability on the AgNW electrode. So, we believe the presence of ribbing structures in the gravure-printed ZnO film was due to the fast drying of the ethanol-based inks, which resulted in improper leveling of ZnO inks

on the top of AgNWs electrodes. Then we used a higher boiling point (117.7 °C) butanol-dispersed ZnO ink. The SEM images of the gravure-printed ZnO films on the AgNW electrodes are shown in Figure 2d. It can be found that though the ribbing structure was not observed, the uniformity of the gravure-printed ZnO film from butanol-based inks was still poor. It is believed that the excessive movement of the ink droplets during the high-speed printing process might be the main reason for the unevenness of the ZnO film. Then, to obtain a ZnO ink with a more suitable volatilization rate, a mixed solvent of ethanol and butanol was utilized. It was found that when ZnO was dispersed in the mixed solvent with 50% butanol and 50% ethanol, the obtained films showed smooth and compact morphology (Figure 2e). To understand the deep reason, the surface tension, contact angle, and viscosity of the three ZnO inks were studied and shown in Figure 2f, Figures S2 and S3, and Table S1, Supporting Information. The results that showed these parameters have slight difference. Therefore, the drying speed should mainly take the responsibility for morphological differences, which was in good agreement with the leveling model of gravure printing (Figure 1).

2.3. Improved the Micro Uniformity and Compactness of the Gravure-Printed ZnO Films Through Using PVP Additive

The ribbing structures of the printed ZnO film were eliminated through using the mixed solvent, which lead to improved uniformity of the macroscopical morphology. However, the microscopic morphology of the ZnO thin film (as shown in Figure S4, Supporting Information) was still loose and uneven. The formation of such a loose and uneven film might be ascribed to the self-aggregation of nanoparticles and low interaction force between ink droplets. To solve this problem, we
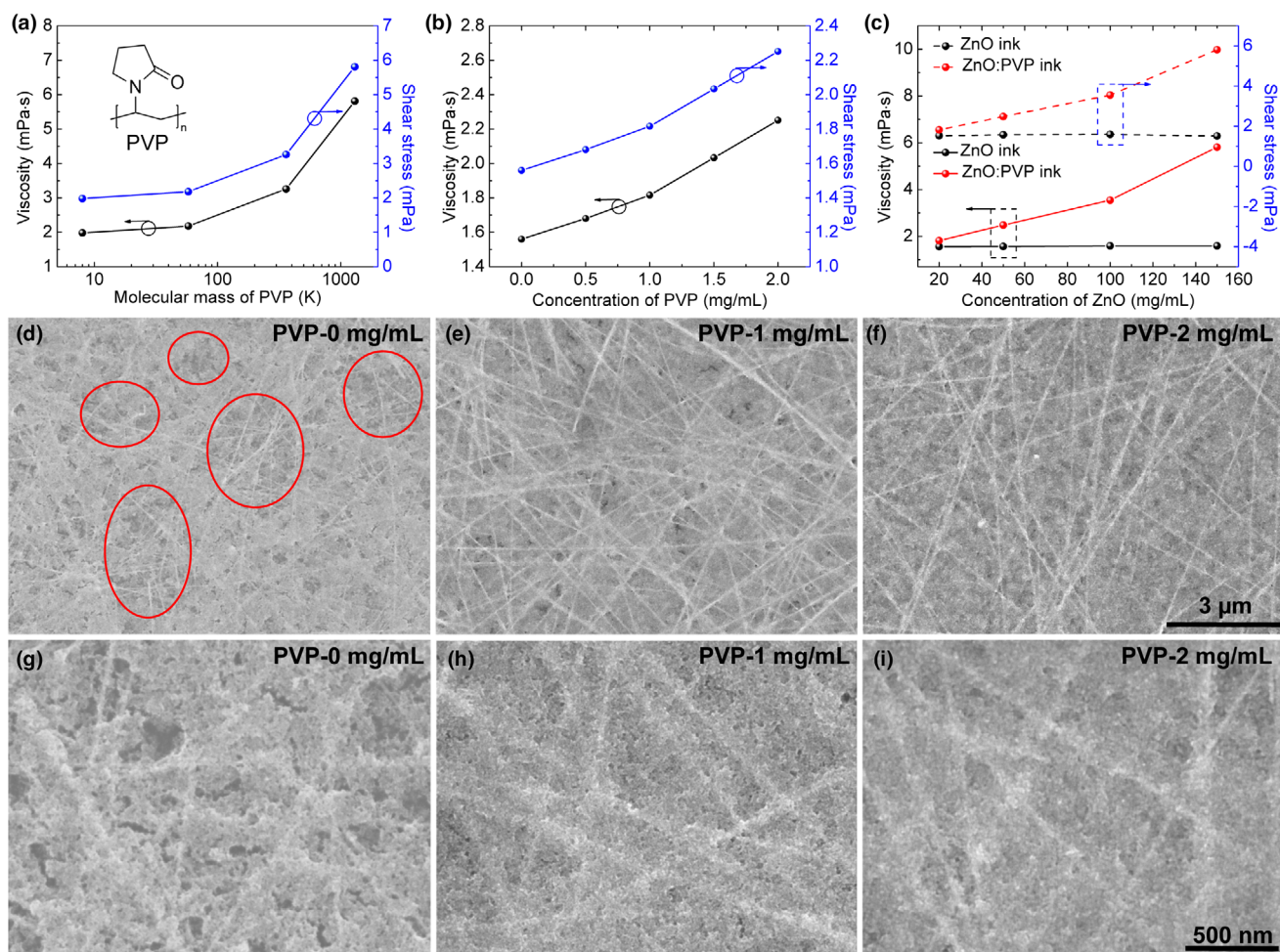
Figure 3. a) Viscosity and shear stress at a shear rate 1 s^{-1} from ZnO:PVP inks with different PVP molecular mass. b) Viscosity and shear stress at a shear rate 1 s^{-1} of the ZnO:PVP inks with different PVP concentrations. c) Viscosity and shear stress at a shear rate 1 s^{-1} from ZnO:PVP and ZnO inks with different ZnO concentrations. d–i) SEM images of the gravure-printed ZnO:PVP films on AgNW electrodes with different PVP concentrations.

introduced a suitable polymer additive in the ZnO inks. Polymers such as polyethyleneimine (PEI), poly (ethylene glycol) (PEG), and polyvinylpyrrolidone (PVP) were selected because the addition of these materials has less effect on the optoelectronic properties of ZnO.[40–42] However, the result (Figure S5, Supporting Information) showed that the viscosity of the ZnO ink only increased from 1.56 to 1.66 mPa·s when the PEI concentration was increased to 2 mg mL^{-1}, suggesting PEI is invalid to regulate the rheological properties of ZnO inks. PEG was also added in ZnO inks, but PEG could not be well dispersed in the mixed solvent of butanol and ethanol. Unlike PEI and PEG, the addition of PVP in the ZnO inks has highly impacted the inks viscosity (as shown in **Figure 3**a, Figure S6, and Table S2, Supporting Information). In addition, with the increase of the molecular mass of PVP, the viscosity and shear stress increased significantly. The introduction of low-molecular mass PVP only caused a slight change in inks viscosity and sheer stress. This result indicated the molecular mass of PVP plays a key role in regulating the rheological properties of the ink. PVP with high molecular mass (1300k) would enhance the entanglement of PVP chains and improve the interaction force within the ink. The effect of concentration of PVP on the rheological properties of ZnO ink showed

that the viscosity of ZnO:PVP ink gradually increased from 1.56 to 2.25 mPa·s as the concentration of PVP increased (Figure 3b, Figure S7, and Table S3, Supporting Information) and the shear stress of the ink increased from 1.56 to 2.25 mPa.

We know the viscosity and shear stress of inks would change gradually during solvent evaporating rather than keeping constant.[28,29] To further explore the change of ink viscosity and shear stress during ink volatilization, we measured rheological parameters of ZnO:PVP with higher concentration. It is found that as the concentration of ZnO and PVP increased, the viscosity of ZnO:PVP ink gradually increased from 1.82 to 5.81 mPa·s, and the shear stress of ink increased from 1.82 to 5.81 mPa (as shown in Figure 3c, Figure S8 and Table S4, Supporting Information). But for ZnO ink without PVP, the ink viscosity and shear stress remained unchanged with the increase of ZnO concentration (as shown in Figure S9 and Table S4, Supporting Information). This result showed that the addition of PVP contributed to the increase of viscosity and shear stress, which would significantly influence the volatilization process and decide the films morphology.

Figure 3d–i shows the SEM images of the gravure-printed ZnO:PVP films on AgNW electrodes with different PVP concentrations. It can be
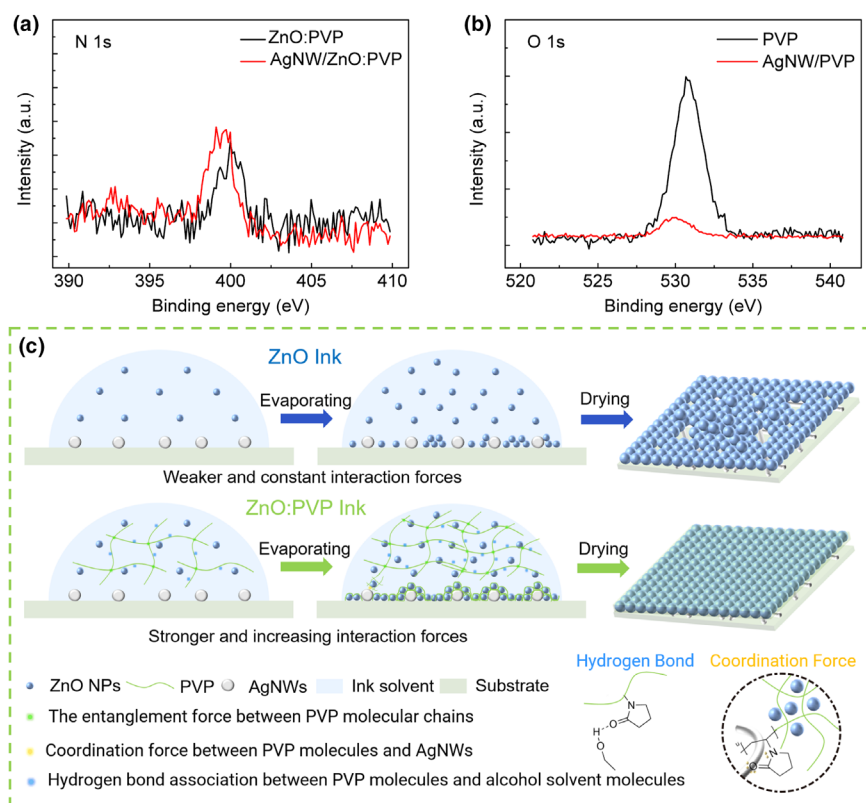
Figure 4. a) XPS spectra of the core level of N 1s in the ZnO:PVP and AgNW/ZnO:PVP films. b) XPS spectra the core level of O 1s in PVP and AgNW/PVP films. c) The mechanism diagram of the gravure-printed ZnO:PVP or ZnO films.

found that with the increase of PVP concentration, the compactness and uniformity of ZnO:PVP thin films are significantly improved. This is mainly because the introduction of PVP significantly enhanced the interaction of inks since the viscosity and shear stress of ZnO inks were increased. The atomic force microscopy (AFM) images of the ZnO:PVP films (Figure S10, Supporting Information) showed that the introduction of PVP in the ZnO ink has significantly reduced the root mean roughness (RMS) from 16.51 to 9.43 nm. In addition, the ZnO:PVP films also showed fewer voids and nanoparticle aggregation, thereby the AgNW electrode was completely covered. The reduced roughness and improved coverage of ZnO:PVP on AgNWs would further facilitate charge transport and enable high performance of devices.

To further understand the interaction between AgNW and ZnO:PVP, the X-ray photoelectron spectroscopy (XPS) of the corresponding films was measured. The XPS spectra of the core level of N 1s in the ZnO:PVP and AgNW/ZnO:PVP films are shown in **Figure 4**a. The binding energy of N 1s in ZnO:PVP red shifted from 400.0 to 399.1 eV after combining with AgNW. The smaller binding energy is owing to the increase of electron cloud density.[43] To eliminate the interference of O elements in ZnO on the O peak position of PVP, the O and N peak positions of PVP and AgNW/PVP films were tested (as shown in Figure S11, Supporting Information and Figure 4b). The binding energy of N 1s and O 1s in PVP moved from 400.2 and 530.7 to 399.2 and 530.1 eV, respectively. These results indicated strong interaction between PVP and Ag. This coordination effect will help ZnO:PVP to wrap the AgNW, which can significantly reduce the probability of short circuits and leakage in the device. The Zn 2p spectra of ZnO

and ZnO:PVP and the N 1s spectra of PVP and ZnO:PVP are shown in Figure S12, Supporting Information. Both the peak positions of Zn 2p and N 1s were unchanged, indicating there is no obvious chemical bonding force between ZnO and PVP.

The formation diagram of the gravure-printed ZnO film from different inks is shown in Figure 4c. The addition of PVP strongly increased the interaction effect of nanoparticles due to the entanglement force between PVP molecular chains and the association of hydrogen bonds between carbonyl groups of PVP molecules and hydroxyl groups of the alcohol solvent molecules. As the solvent volatilized, the entanglement and hydrogen-bond effects gradually increased with the increase of PVP concentration. Therefore, the viscosity and shear stress of ZnO:PVP ink gradually increased. Due to the strong interaction between PVP molecules and AgNWs, ZnO:PVP NPs would uniformly deposit on the top of AgNWs during printing, which is essential to totally cover the AgNWs and reduce the risk of device leakage current. In all, the introduction of PVP into the ZnO ink significantly increased the interaction between solutes, improved the rheological properties of ink, and meanwhile enhanced the interaction force between ZnO and AgNWs, thus significantly improving the uniformity and compactness of the films.

2.4. Properties of Large-Area Gravure-Printed AgNWs/ZnO:PVP Films

The distribution of ZnO and PVP in printed films takes a crucial role in the photoelectronic property of the films. Thus, time-of-flight secondary ion mass spectrometry (ToF-SIMS) of the ZnO:PVP films was studied. **Figure 5**a and Figure S13, Supporting Information show the surface ToF-SIMS mapping of ZnO and CN^- in ZnO:PVP films. As showed by the ToF-SIMS mapping, we found that the signal of CN^- was very uniformly distributed in the ZnO:PVP films. Since the signal of CN^- originates from the PVP molecule, this result proves that PVP was uniformly distributed on the surface of the ZnO:PVP without aggregation. The uniform distribution of PVP in the printed film is beneficial for improving the electrical properties of the printed ZnO:PVP films. The ToF-SIMS depth profiles of ZnO and CN^- in the ZnO:PVP films (Figure 5b) showed the distribution of PVP and ZnO in the vertical direction is overall uniform, with slight enrichment of PVP on the film surface within 5 nm. From the 3D ToF-SIMS images of ZnO:PVP (as shown in Figure S14, Supporting Information), it can also be observed that both PVP and ZnO are uniformly distributed throughout the ZnO:PVP film without obvious aggregation, which will ensure good conduction and optical transmission properties of the ZnO:PVP film.

The influence of PVP concentration on the transmittance of ZnO films was investigated (as shown in Figure 5c). It can be found that the transmission spectra of ZnO films with different PVP concentrations are nearly coincident, suggesting the addition of PVP has
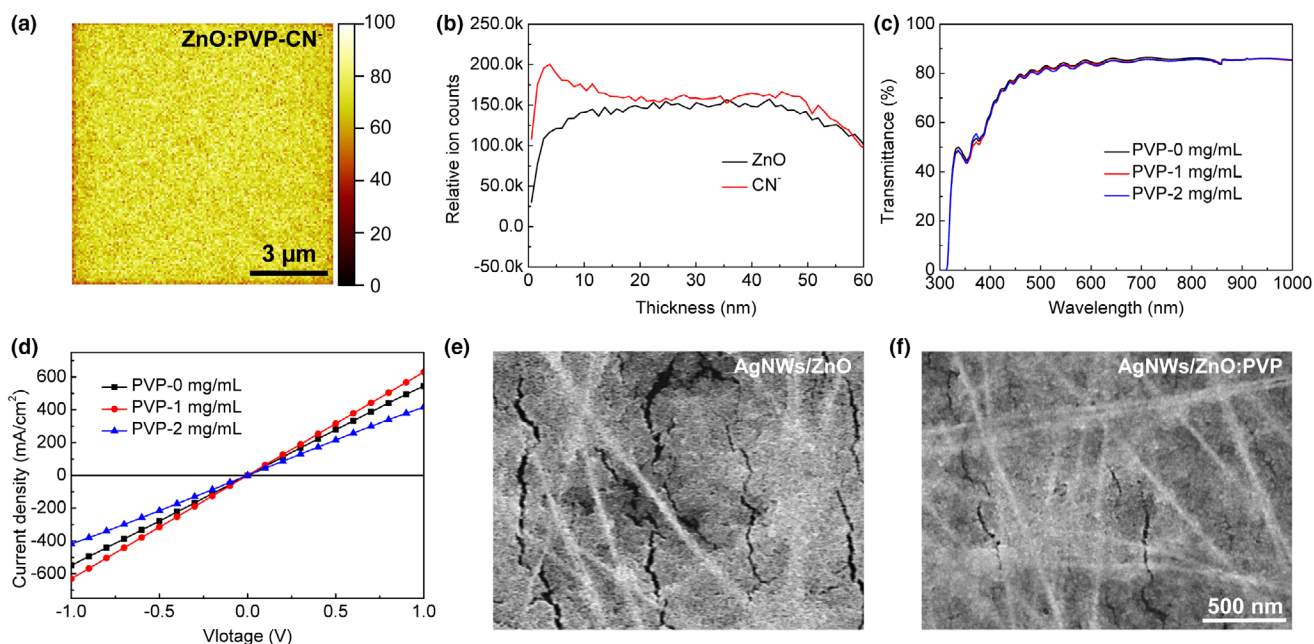
Figure 5. a) Surface ToF-SIMS mapping of CN⁻ in ZnO:PVP films. b) ToF-SIMS depth profiles of ZnO and CN⁻ in ZnO:PVP films. c) Transmittance spectra of the gravure-printed ZnO:PVP films on AgNW electrodes from ZnO:PVP inks with different PVP concentrations. d) J–V curves of the ITO/ZnO:PVP films (110 nm)/Al (100 nm) devices with different PVP concentrations. e, f) SEM images of the printed films after 1000 bending cycles with a bending radius of 3 mm: e) AgNWs/ZnO film and f) AgNWs/ZnO:PVP film.

negligible influence on optical transmission. This result was proved by the excellent optical transparency of PVP in the range of 300–1000 nm (as shown in Figure S15, Supporting Information). The conduction of these printed films was evaluated according to the current density–voltage (J–V) curves of ZnO:PVP films (Figure 5d and Figure S16, Supporting Information). It can be found that with the increase of PVP concentration, the conductivity of ZnO:PVP first increased and then decreased, with the concentration of 1 mg mL⁻¹ as a saturation. This is because the addition of an appropriate amount of PVP can significantly improve the compactness and uniformity of the ZnO film, leading to more effective contact between the adjacent ZnO nanoparticles, and thereby enabling the charge transporting among the adjacent ZnO nanoparticles. While with a higher concentration of PVP, the conduction of ZnO:PVP inversely decreased because of the insulation nature of PVP. We further studied the influence of PVP on the bending performance of the ZnO films (as shown in Figure 5e,f). The printed ZnO and ZnO:PVP films were bent for 1000 cycles with a bending radius of 3.5 mm. As shown in the SEM images, there were lots of big cracks in the pure ZnO film after bending. However, in the ZnO:PVP films, only a few small cracks were found after the same bending cycle. The improvement of mechanical durability of ZnO:PVP relative to ZnO might be attributed to two aspects. First, the ZnO film is more loose and rough, thereby it is easier to form cracks during continuous bending, while the ZnO:PVP film was more compact and smooth. Second, the flexible nature of PVP would enhance the bending durability of the composite films.

2.5. Application of Gravure-Printed ZnO Films in the Flexible OSCs

Figure 6a shows the device structure of the flexible OSCs based on the gravure-printed AgNWs and ZnO:PVP films and the molecular

structure of electron donor PM6 and electron acceptor Y6. Figure 6b shows the J–V curves of the devices based on the gravure-printed ZnO:PVP films with different PVP concentrations. The corresponding performance parameters are listed in **Table 1**. It can be found that with the increase of PVP content, device open-circuit voltage (V_{OC}) kept constant, while the short circuit current densities (J_{SC}), fill factors (FF), and power conversion efficiency (PCE) of the device firstly increased and then decreased. As an optimization, the highest device efficiency of 15.01% was obtained, with a V_{OC} of 0.821 V, a J_{SC} of 24.58 mA cm⁻², and a FF of 74.45% when the concentration of PVP was 1 mg mL⁻¹. With the addition of appropriate amount of PVP in the ZnO inks, the printed films became more dense and uniform, thereby the conduction of ZnO:PVP films improved. Therefore, both J_{SC} and FF of the device improved relative to the device with pure ZnO ETL. When the concentration of PVP was higher than 2 mg/mL, the conductivity of the ZnO:PVP film was significantly reduced (Figure 5d), and lead to larger charge transfer resistance, thereby resulting in a decrease of J_{SC} and Figure S17, Supporting Information shows the external quantum efficiency (EQE) spectra of these devices. The integrated currents calculated over the EQE spectra were in good agreement with the J–V curves. We further studied the influence of PVP on the bending performance of the flexible OSCs (as shown in Figure S18, Supporting Information). It was interesting to find that both the ZnO and ZnO:PVP ETL-based FOSCs showed similar bending durability though the ZnO:PVP films that have much better durability. That would be because the cover of the organic photoactive layer on the top of ZnO ETLs can effectively restrain the formation of cracks in the whole device. Consequently, both the ZnO and ZnO:PVP ETL-based OFSCs exhibited higher than 95% of initial efficiency after 1000 bending cycles with a radius of 3.5 mm.

The printing window of composite solvent-dispersed ZnO:PVP inks and the working thickness of the printed films are two key aspects
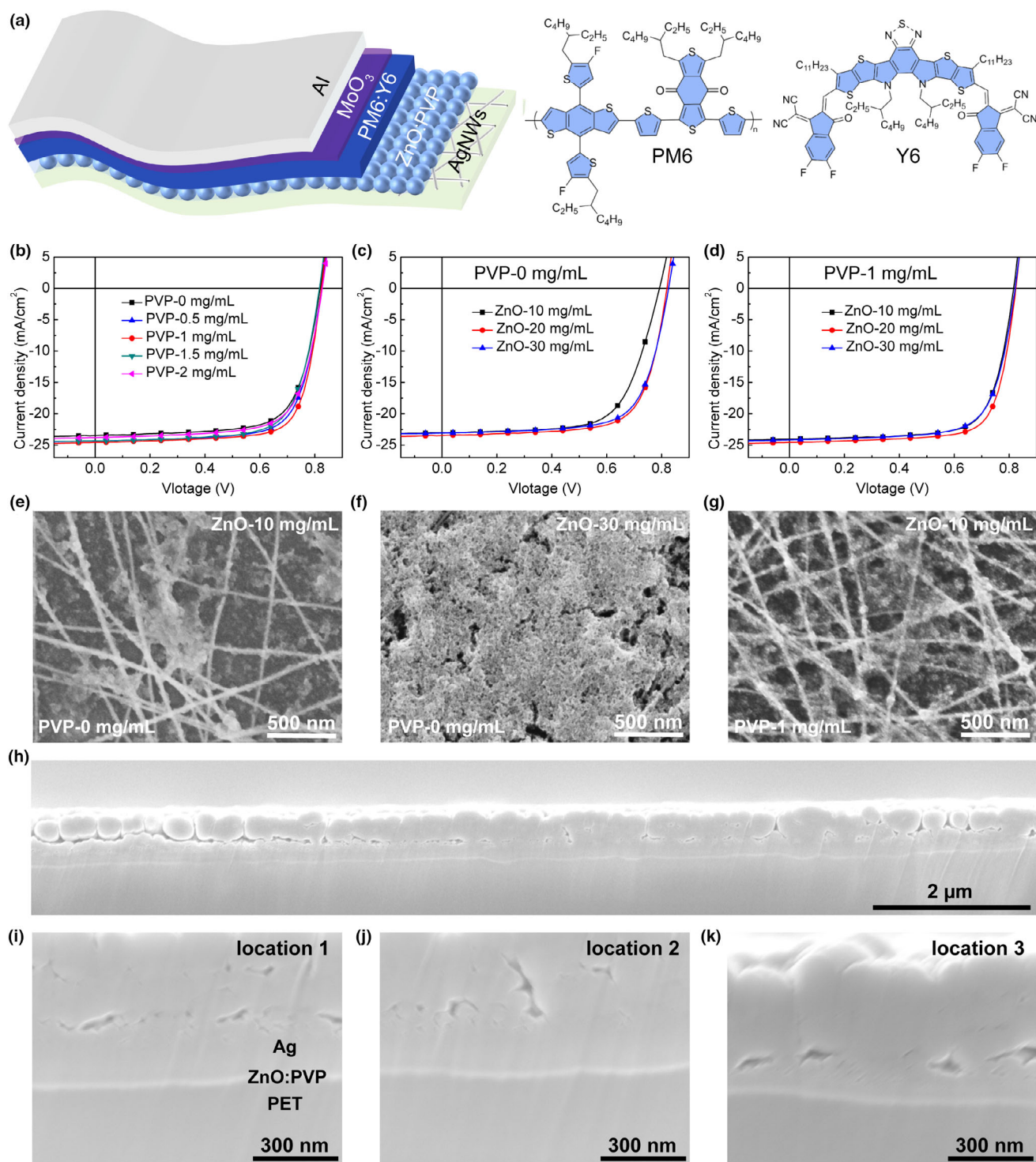
Figure 6. a) Device structure of the flexible OSCs and the molecular structure of the donor PM6 and the acceptor Y6. b) J–V curves of the devices based on the gravure-printed ZnO:PVP films with different PVP concentrations. c, d) J–V curves of the devices based on c) the gravure-printed ZnO films and d) the gravure-printed ZnO:PVP films with different ZnO concentrations. e, f) SEM images of the gravure-printed ZnO films on AgNW electrodes with different ZnO concentrations. g) SEM image of the gravure-printed ZnO:PVP films on AgNW electrodes. h–k) SEM cross-section images of the gravure-printed ZnO:PVP films on PET.

Table 1. Device performance of the PM6:Y6 solar cells based on the gravure-printed ZnO:PVP films with different PVP concentrations.

Concentration of PVP (mg mL^{-1})	V_{OC} (V)	J_{SC} (mA cm^{-2})	FF (%)	PCE[a] (%)
0	0.820	23.49	70.89	13.65 (13.23 ± 0.29)
0.5	0.821	24.35	72.34	14.47 (14.21 ± 0.20)
1	0.821	24.58	74.45	15.01 (14.71 ± 0.23)
1.5	0.820	24.31	72.17	14.39 (14.13 ± 0.21)
2	0.824	23.79	71.06	14.03 (13.63 ± 0.26)

[a]The average performance parameters were calculated from 20 individual devices.

that decide the large-area printability and practicability. Thus, we regulated the film thickness varying from 30 to 100 nm through regulating the ink concentrations. Figure 6c,d shows the J–V curves of the devices based on the gravure-printed ZnO and gravure-printed ZnO:PVP films with different ZnO thicknesses, and the corresponding performance parameters are listed in **Table 2**. It can be found that in the device with pure ZnO ETL, the device efficiency dropped drastically from 13.23% to 11.29% when the ZnO concentrations reduced from 20 mg mL^{-1} (with a thickness of 65 nm) to 10 mg mL^{-1} (with a thickness of 35 nm). This is because the coverage of ZnO nanoparticles on the AgNW electrode becomes seriously inhomogeneous with the decreasing ZnO concentration (as shown in Figure 6e and Figure S19a, Supporting Information). Part of the AgNWs was not covered by ZnO, which may be the main reason of the device leakage current. When the concentration of ZnO further increased to 30 mg mL^{-1} (with a thickness of 103 nm), the average efficiency was also reduced to 12.73%. This is due to the appearance of some obvious cracks in the ZnO film with the increase of ZnO concentration, which would restrict the charge transport at the cathode. For the ZnO:PVP composite films, we found the device performance slightly changed from 14.71% to 13.96% as the ink concentration varied from 10 (with a thickness of 33 nm) to 30 mg mL^{-1} (with a thickness of 98 nm). It can also be seen from Figure 6g and Figure S19b,c, Supporting Information that the ZnO:PVP films were uniform and compact with ZnO concentration varying from 10 to 30 mg mL^{-1}, which might be ascribed to three aspects. First of all, the introduction of PVP has significantly increased the viscosity and shear stress of ZnO ink, which indicated enhanced interaction force between the ZnO nanoparticles and lead to a more uniform distribution of nanoparticles. Additionally, the strong interaction between

PVP molecules and AgNWs would lead to the wrap of AgNWs by ZnO:PVP. Finally, the introduction of PVP can significantly increase the flexibility of ZnO films and inhibit the generation of film cracks. Figure S20, Supporting Information shows the EQE spectra of these devices. The integrated currents calculated over the EQE spectra are in good agreement with the J–V curves. The cross-sectional SEM images (Figure 6h–k) of the printed ZnO:PVP films showed the gravure-printed films were extremely uniform even though the thickness was only around 30 nm. Herein, it should be noted that a thin Ag layer was thermal evaporated on the top ZnO:PVP to improve the conduction of the films and clearly show the thickness of the printed films. We know the working thickness and printing window are important evaluating factors for roll-to-roll printing, which decides the printing reproducibility. In general, high working thickness is favored to improve reproducibility. The gravure-printed ZnO:PVP films showed relatively high working thickness from 30 to 100 nm. Besides, we also demonstrated the superior thickness control accuracy of the ZnO:PVP film through gravure printing, indicating great promise for roll-to-roll large-area fabrication.

Generally, ZnO ETL was fabricated through spin-coating for OSCs usage. The large centrifugal force during spin-coating can enable the formation of homogenous films. However, spin-coating is not compatible with the fabrication of large-area films. Here, we compared the performance of the flexible devices with spin-coated and gravure-printed ZnO:PVP ETLs. We prepared the ZnO:PVP composite films with a size of 28 × 9 cm^2 by gravure printing on the AgNW electrode, and the ZnO:PVP composite films with a size of 5 × 4 cm^2 by spin coating (as shown in **Figure 7**a). Figure 7b shows a curled gravure-printed PET/AgNW/ZnO:PVP film. Eight regions from two large-area gravure-printed (ZnO:PVP-GP, 28 × 9 cm^2) films and four regions from four spin-coated (ZnO:PVP-SC, 5 × 4 cm^2) films were selected as substrates for the 1 cm^2 flexible devices. The statistical distribution of device efficiency is shown in Figure 7c. It can be found that most of the ZnO:PVP-SC devices were short circuits or leakage current, which was believed to be due to poor coverage of ZnO:PVP-SC on the top of AgNWs. In contrast, the ZnO:PVP-GP devices showed an average performance of about 14% without device leakage current or short circuit. Figure 7d shows the J–V curves of the 1 cm^2 devices based on ZnO:PVP-SC and on ZnO:PVP-GP films. The corresponding performance parameters are listed in **Table 3**. The PCE of the 1 cm^2 PM6:Y6 flexible OSCs with ZnO:PVP-GP films reached 14.36%. In contrast, the PCE of the 1 cm^2 OSCs with ZnO:PVP-SC films was only 13.43%. The J_{SC} and FF of the devices were significantly lower than those of the ZnO:PVP-GP-based cells. This is mainly because the uniformity of the

Table 2. Device performance of the PM6:Y6 solar cells based on the gravure-printed ZnO and ZnO:PVP films with different ZnO concentrations.

Concentration of PVP (mg mL^{-1})	Concentrtion of ZnO (mg mL^{-1})	Thickness (nm)	V_{OC} (V)	J_{SC} (mA cm^{-2})	FF (%)	PCE[a] (%)
0	10	35 ± 13	0.790	23.06	66.84	12.18 (11.29 ± 0.79)
	20	65 ± 15	0.820	23.49	70.89	13.65 (13.23 ± 0.29)
	30	103 ± 18	0.819	23.07	69.98	13.22 (12.73 ± 0.35)
1	10	33 ± 6	0.820	24.06	72.79	14.36 (14.09 ± 0.18)
	20	61 ± 9	0.821	24.58	74.45	15.01 (14.71 ± 0.23)
	30	98 ± 13	0.820	24.19	71.56	14.19 (13.96 ± 0.21)

[a]The average performance parameters were calculated from 20 individual devices.

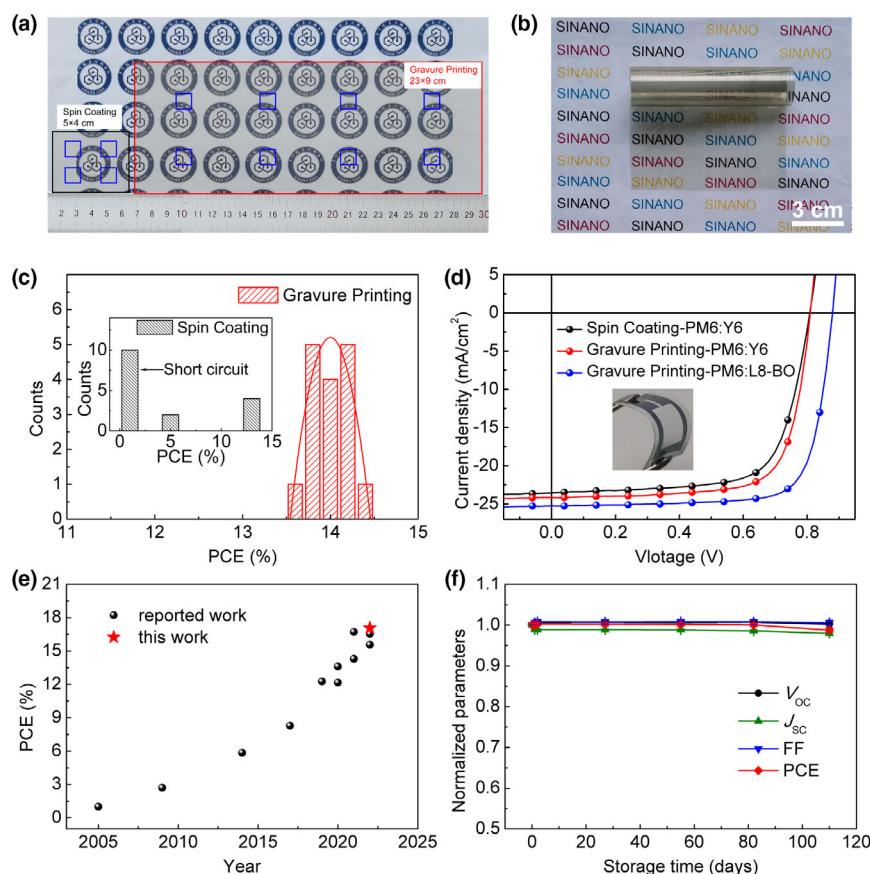**Figure 7.** a) Photographs of the PET/AgNWs/ZnO:PVP-SC (5×4 cm^2) and PET/AgNWs/ZnO:PVP-GP (28×9 cm^2) films. b) Photograph of the curled PET/AgNWs/ZnO:PVP-GP film. c) PCE histogram of the 1 cm^2 flexible devices based on ZnO:PVP-GP and on ZnO:PVP-SC (the inset) films. d) J–V curves of the 1 cm^2 flexible devices based on ZnO:PVP-SC and on ZnO:PVP-GP films. e) A summary of PCEs of large-area flexible organic solar cells with area ~1 cm^2.[7,18,30,37,39,46–53] f) Shelf stability of the 1cm^2 PM6:L8-BO devices based on PET/AgNWs /ZnO:PVP-GP films that stroded in a nitrogen glove box.

Table 3. Device performance of the 1 cm^2 flexible devices based on ZnO: PVP-SC and on ZnO:PVP-GP films.

ETL	Active layer	V_{OC} (V)	J_{SC} (mA cm^{-2})	FF (%)	PCE[a] (%)
ZnO:PVP-SC	PM6:Y6	0.810	23.56	70.36	13.43 (4.50 $\pm$ 5.25)
ZnO:PVP-GP	PM6:Y6	0.810	24.17	73.35	14.36 (14.00 $\pm$ 0.21)
	PM6:L8-BO	0.879	25.25	76.81	17.07 (16.83 $\pm$ 0.16)

[a]The average performance parameters were calculated from 16 individual devices.

gravure-printed ZnO:PVP film was much better than that of the spin-coated film (as shown in Figure S21, Supporting Information). In addition, flexible OSCs with PM6:L8-BO heterojunction layer were also fabricated. Figure S22, Supporting Information shows the molecular structure of electron acceptor L8-BO. The J–V curves and the corresponding performance parameters are shown in Figure 7d and Table 3. Notably, the PCE of the 1 cm^2 flexible OSCs ZnO:PVP-GP ETL reached 17.07%, with a V_{OC} of 0.879 V, a J_{SC} of 25.25 mA cm^{-2}, and a FF of 76.81%. To the best of our knowledge, a PCE of 17.07% is the highest

reported value to date for the 1 cm^2 flexible OSCs (statistical data as shown in Figure 7e and Table S5, Supporting Information).[17,27,43–53] The integrated currents calculated over the EQE spectra (Figure S23, Supporting Information) are in good agreement with the J–V curves. This observation demonstrated the gravure-printed ZnO:PVP films have prominent advantages in large-area flexible OSCs. Then, we further investigated the shelf stability of the 1 cm^2 PM6:L8-BO flexible devices in a nitrogen glove box. Figure 7f shows the variation of the performance parameters of the flexible devices with the storage time. It can be seen from the figure that PCE maintained 98.75% of the initial value after 110 days of storage. In the first 50 h, J_{SC} decreased slightly, and the V_{OC} and FF increased slightly. After 50 h, the performance parameters of the device remained stable during higher than 104 days of storage, indicating that FOSCs can maintain long-term stability.

3. Conclusion

In summary, we proposed a strategy to manipulate the macroscopic and microscopic morphology of large-area gravure-printed ZnO films. The ink leveling property of the ZnO ink was regulated through using a composite solvent, and the film ribbing structure was eliminated. With the introduction of PVP, the rheological properties of the ink, including viscosity and shear stress, were improved, leading to the formation of large-area printed ZnO:PVP films (28×9 cm^2) with excellent compactness, uniformity, conductivity, and bending performance. With the large-area printed ZnO:PVP ETL, 1 cm^2 flexible OSCs with PM6:Y6 and PM6:L8-BO active layers achieved 14.34% and 17.07%, respectively. The utilization of composite solvent-dispersed ZnO:PVP also significantly enlarged the printing window of the nanoinks, so that the thickness of ZnO:PVP film can regulate from 30 to 100 nm without obvious performance decrease. All these results suggested the gravure-printed ZnO: PVP films had high performance and excellent large-area uniformity and proved gravure printing is a feasible route to fabricate large-area flexible OSCs.

4. Experimental Section

Materials: PM6 and Y6 were purchased from Solarmer Materials Inc. L8-BO was purchased from Hyper Inc. PVP with the molecule weight (MW) of 8k, 58k, and 1300k was purchased from J&K Scientific, and with the MW of 360k was purchased from Adamas. Polyethyleneimine (PEI, branched, 30 wt.% in H$_2$O) with the MW of 10k and poly (ethylene glycol) (PEG) with the MW of 20k were purchased from J&K Scientific. AgNW inks (10 mg mL^{-1} in H$_2$O or IPA with an average diameter of ≈25 nm and a length of ≈25 μm) were purchased from Zhejiang Kechuang Advanced Materials Co., Ltd. ZnO nanoparticles were synthesized as described by Beek et al.[54] 1-chloronaphthalene (CN, 97%) was purchased

from TCI. 1,8-diiodooctane (DIO) was purchased from J&K Scientific. Surface hydrophilic PET was purchased from Toyobo (Osaka, Japan).

PET/AgNWs/ZnO:PVP film fabrication: PET/AgNWs electrodes were prepared by the gravure printing method according to our previous report.[30] By diluting and mixing the water-dispersed and isopropanol (IPA)-dispersed AgNW inks, the AgNW with a concentration of 5 mg mL^{-1} is dispersed in a mixed solvent (IPA:H$_2$O = 7:3, v/v). To obtain the PET/AgNWs electrodes, the AgNW inks were printed on PET substrates using a gravure printing proof (D&R Lab Gravure Printer G-1100S; Suzhou D&R Instrum Co., Ltd.) at a speed of 50 m min^{-1}. The cavity volume per an area of the gravure roller was 13 mL m^{-2} with 50 lines cm^{-1}. The AgNWs were annealed at 120 °C for 10 min in an oven. Then, AgNW electrodes with different square resistances of 17 and 10 Ω sq^{-1} were obtained, which were used to for 0.04 and 1 cm^2 OSCs. PVP was dissolved into ethanol to get a PVP solution (10 mg mL^{-1}). First, the synthesized ZnO NPs were dispersed in butanol and ethanol solvents, respectively, and the two kinds of inks were mixed with different solvent ratios to obtain composite solvent-based inks. Finally, the butanol and ethanol composite solvent-based ZnO NPs inks and the PVP ethanol solution were mixed to obtain ZnO:PVP inks with different PVP and different ZnO concentrations. To obtain the PET/AgNWs/ZnO:PVP films, first, the AgNW electrode was treated in an oxygen plasma chamber for 2 min. Then, the ZnO:PVP ink was printed on PET/AgNWs electrodes using a gravure printing proof (D&R Lab Gravure Printer G-1100S; Suzhou D&R Instrum Co., Ltd.) at a speed of 50 m min^{-1}. The cavity volume per an area of the gravure roller was 13 mL m^{-2} with 50 lines cm^{-1}. The PET/AgNWs/ZnO:PVP films were annealed at 120 °C for 10 min in an oven.

OSCs fabrication: Flexible OSCs with an inverted PET/AgNWs/ZnO or ZnO:PVP/PM6:Y6/MoO$_3$/Al were fabricated on the PET/AgNWs/ZnO or ZnO:PVP film. For spin-coated ZnO devices, ZnO nanoparticles were spin-coated on top of the PET/AgNW at 1000 round/min for 60 s and annealed at 120 °C for 10 min in an N$_2$-filled glove box. PM6:Y6 (D:A = 1:1.2, 16 mg mL^{-1} in total) was dissolved in chloroform (CF) with the solvent additive of CN (0.5%, v/v). Subsequently, the PM6:Y6 was spin-coated at 2000 round/min for 30 s on the ZnO layer and thermally annealed at 100 °C for 10 min. PM6:L8-BO (D:A = 1:1.2, 17.6 mg mL^{-1} in total) was dissolved in chloroform (CF) with the solvent additive of DIO (0.25%, v/v). Subsequently, the PM6:L8-BO solution was spin-coated at 3000 round/min for 30 s on the ZnO layer and thermally annealed at 100 °C for 10 min. Finally, a MoO$_3$ layer (10 nm) and an Al layer (200 nm) were deposited on the active layer by vacuum evaporation at 3 × 10^{-4} Pa.

Characterization: The surface tension of ZnO or ZnO:PVP inks was measured at 25 °C using a Kibron EZ-Piplus Surface Tensiometer (Finland). The viscosity of ZnO and ZnO:PVP inks was measured at 25 °C using a Malvern Kinexus rheometer (Malvern, UK). The SEM images of the PET/AgNWs/ZnO or ZnO:PVP films were measured using a Hitachi S4800 (Tokyo, Japan). The transmittance of the PET/AgNWs/ZnO or ZnO:PVP films was measured using a Lambada 750 UV–vis–NIR spectrophotometer (PerkinElmer, Waltham, USA). The sheet resistance of the AgNW electrodes was measured using a ST-2258C four-probe instrument (Suzhou Jingge Electronic, Suzhou, China). The roughness of the AgNW films was measured using AFM (Veeco Dimension 3100, New York, USA) in tapping mode. The thickness of the gravure ZnO and ZnO:PVP films was measured by Bruker DektakXT probe-type surface profilometer. The XPS spectra of ZnO, PVP, ZnO:PVP, AgNW/PVP, and AgNW/ZnO:PVP films were measured using an ESCALAB 250Xi spectrometer with a monochromatic Al Kα X-ray source with an overall energy space of ΔE = 0.1 eV at Vacuum Interconnected Nanotech Workstation (Nano-X) of SINANO. TOF-SIMS images of the ZnO and ZnO:PVP films were obtained using a ToF-SIMS5-100 at Vacuum Interconnected Nanotech Workstation (Nano-X) of SINANO. The J–V measurements were performed in a nitrogen glove box with a Keithley 2400 source meter under simulated AM 1.5 G solar illumination (100 mW cm^{-2}) generated by a Zolix SS150 solar simulator. EQE values were measured under simulated 1 sun operation conditions using bias light from a 532 nm solid-state laser (Changchun New Industries, MGL-III-532).

Conflict of Interest

There is no conflict of interest involved in the work.

Supporting Information

Supporting Information is available from the Wiley Online Library or from the author.

[1] D. Meng, R. Zheng, Y. Zhao, E. Zhang, L. Dou, Y. Yang, *Adv. Mater.* **2022**, *34*, e2107330.

[2] C. Li, J. Zhou, J. Song, J. Xu, H. Zhang, X. Zhang, J. Guo, L. Zhu, D. Wei, G. Han, J. Min, Y. Zhang, Z. Xie, Y. Yi, H. Yan, F. Gao, F. Liu, Y. Sun, *Nat. Energy* **2021**, *6*, 605.

[3] L. Zuo, S. B. Jo, Y. Li, Y. Meng, R. J. Stoddard, Y. Liu, F. Lin, X. Shi, F. Liu, H. W. Hillhouse, D. S. Ginger, H. Chen, A. K. Jen, *Nat. Nanotechnol.* **2022**, *17*, 53.

[4] Y. Wei, Z. Chen, G. Lu, N. Yu, C. Li, J. Gao, X. Gu, X. Hao, G. Lu, Z. Tang, J. Zhang, Z. Wei, X. Zhang, H. Huang, *Adv. Mater.* **2022**, *34*, e2204718.

[5] H. Zhao, B. Lin, J. Xue, H. B. Naveed, C. Zhao, X. Zhou, K. Zhou, H. Wu, Y. Cai, D. Yun, Z. Tang, W. Ma, *Adv. Mater.* **2022**, *34*, e2105114.

[6] Y. Zhang, K. Liu, J. Huang, X. Xia, J. Cao, G. Zhao, P. W. K. Fong, Y. Zhu, F. Yan, Y. Yang, X. Lu, G. Li, *Nat. Commun.* **2021**, *12*, 4815.

[7] J. Yuan, Y. Zhang, L. Zhou, G. Zhang, H.-L. Yip, T.-K. Lau, X. Lu, C. Zhu, H. Peng, P. A. Johnson, M. Leclerc, Y. Cao, J. Ulanski, Y. Li, Y. Zou, *Joule* **2019**, *3*, 1140.

[8] L. Zhu, M. Zhang, J. Xu, C. Li, J. Yan, G. Zhou, W. Zhong, T. Hao, J. Song, X. Xue, Z. Zhou, R. Zeng, H. Zhu, C. C. Chen, R. C. I. MacKenzie, Y. Zou, J. Nelson, Y. Zhang, Y. Sun, F. Liu, *Nat. Mater.* **2022**, *21*, 656.

[9] Y. Cai, Q. Li, G. Lu, H. S. Ryu, Y. Li, H. Jin, Z. Chen, Z. Tang, G. Lu, X. Hao, H. Y. Woo, C. Zhang, Y. Sun, *Nat. Commun.* **2022**, *13*, 2369.

[10] Y. Y. Jiang, X. Y. Dong, L. L. Sun, T. F. Liu, F. Qin, C. Xie, P. Jiang, L. Hu, X. Lu, X. M. Zhou, W. Meng, N. Li, C. J. Brabec, Y. H. Zhou, *Nat. Energy* **2022**, *7*, 352.

[11] P. Jiang, J. Chen, F. Qin, T. Liu, S. Xiong, W. Wang, C. Xie, X. Lu, Y. Jiang, H. Han, Y. Zhou, *Angew. Chem. Int. Ed.* **2022**, *61*, e202208815.

[12] J. Xue, H. Zhao, B. Lin, Y. Wang, Q. Zhu, G. Lu, B. Wu, Z. Bi, X. Zhou, C. Zhao, G. Lu, K. Zhou, W. Ma, *Adv. Mater.* **2022**, *34*, e2202659.

[13] F. Yang, Y. T. Huang, Y. W. Li, Y. F. Li, *npj Flex. Electron.* **2021**, *5*, 30.

[14] L. W. T. Ng, S. W. Lee, D. W. Chang, J. M. Hodgkiss, D. Vak, *Adv. Mater. Technol.* **2022**, *7*, 2101556.

[15] C. Liu, C. Xiao, C. Xie, W. Li, *Nano Energy* **2021**, *89*, 106399.

[16] H. Chen, R. Zhang, X. Chen, G. Zeng, L. Kobera, S. Abbrent, B. Zhang, W. Chen, G. Xu, J. Oh, S.-H. Kang, S. Chen, C. Yang, J. Brus, J. Hou, F. Gao, Y. Li, Y. Li, *Nat. Energy* **2021**, *6*, 1045.

[17] G. Wang, J. Zhang, C. Yang, Y. Wang, Y. Xing, M. A. Adil, Y. Yang, L. Tian, M. Su, W. Shang, K. Lu, Z. Shuai, Z. Wei, *Adv. Mater.* **2020**, *32*, e2005153.

[18] H. J. Li, S. Q. Liu, X. T. Wu, Q. C. Qi, H. Y. Zhang, X. C. Meng, X. T. Hu, L. Ye, Y. W. Chen, *Energy Environ. Sci.* **2022**, *15*, 2130.

[19] J. E. Carlé, M. Helgesen, O. Hagemann, M. Hösel, I. M. Heckler, E. Bundgaard, S. A. Gevorgyan, R. R. Søndergaard, M. Jørgensen, R. García-Valverde, S. Chaouki-Almagro, J. A. Villarejo, F. C. Krebs, *Joule* **2017**, *1*, 274.

[20] F. C. Krebs, T. Tromholt, M. Jorgensen, *Nanoscale* **2010**, *2*, 873.

[21] F. C. Krebs, *Sol. Energy Mater. Sol. Cells* **2009**, *93*, 394.

[22] M. Valimaki, P. Apilo, R. Po, E. Jansson, A. Bernardi, M. Ylikunnari, M. Vilkman, G. Corso, J. Puustinen, J. Tuominen, J. Hast, *Nanoscale* **2015**, *7*, 9570.

[23] Y. Y. Kim, T. Y. Yang, R. Suhonen, A. Kemppainen, K. Hwang, N. J. Jeon, J. Seo, *Nat. Commun.* **2020**, *11*, 5146.

[24] Y. Y. Kim, T. Y. Yang, R. Suhonen, M. Valimaki, T. Maaninen, A. Kemppainen, N. J. Jeon, J. Seo, *Adv. Sci.* **2019**, *6*, 1802094.

[25] M. Valimaki, E. Jansson, P. Korhonen, A. Peltoniemi, S. Rousu, *Nanoscale Res. Lett.* **2017**, *12*, 117.

[26] C. Kapnopoulos, E. D. Mekeridis, L. Tzounis, C. Polyzoidis, A. Zacharidis, S. Tsimikli, C. Gravalidis, A. Laskarakis, N. Vouroutzis, S. Logothetidis, *Sol. Energy Mater. Sol. Cells* **2016**, *144*, 724.

[27] Z. Wang, Y. Han, L. Yan, C. Gong, J. Kang, H. Zhang, X. Sun, L. Zhang, J. Lin, Q. Luo, C. Q. Ma, *Adv. Funct. Mater.* **2020**, *31*, 2007276.

[28] G. Hernandez-Sosa, N. Bornemann, I. Ringle, M. Agari, E. Dörsam, N. Mechau, U. Lemmer, *Adv. Funct. Mater.* **2013**, *23*, 3164.

[29] G. Grau, J. Cen, H. Kang, R. Kitsomboonloha, W. J. Scheideler, V. Subramanian, *Flex. Print. Electron.* **2016**, *1*, 023002.

[30] C. H. Liu, C. Y. Xiao, W. W. Li, *J. Mater. Chem. C* **2021**, *9*, 14093.

[31] Z. Liang, Q. Zhang, L. Jiang, G. Cao, *Energy Environ. Sci.* **2015**, *8*, 3442.

[32] B. Liu, Y. Han, Z. Li, H. Gu, L. Yan, Y. Lin, Q. Luo, S. Yang, C.-Q. Ma, *Sol. RRL* **2020**, *5*, 2000638.

[33] Y. Han, H. Dong, W. Pan, B. Liu, X. Chen, R. Huang, Z. Li, F. Li, Q. Luo, J. Zhang, Z. Wei, C. Q. Ma, *ACS Appl. Mater. Interfaces* **2021**, *13*, 17869.

[34] P. Fan, D. Y. Zhang, Y. Wu, J. S. Yu, T. P. Russell, *Adv. Funct. Mater.* **2020**, *30*, 2002932.

[35] R. Szentgyörgyvölgyi, in *Printing on polymers* (Eds: J. Izdebska, S. Thomas), William Andrew Publishing, Oxford **2016**, 199–215.

[36] Y. Yu, R. Sun, T. Wang, X. Yuan, Y. Wu, Q. Wu, M. Shi, W. Yang, X. Jiao, J. Min, *Adv. Funct. Mater.* **2020**, *31*, 2008767.

[37] Z. Peng, K. Xian, Y. Cui, Q. Qi, J. Liu, Y. Xu, Y. Chai, C. Yang, J. Hou, Y. Geng, L. Ye, *Adv. Mater.* **2021**, *33*, 2106732.

[38] J. Wan, L. Zeng, X. Liao, Z. Chen, S. Liu, P. Zhu, H. Zhu, Y. Chen, *Adv. Funct. Mater.* **2021**, *32*, 2107567.

[39] C. E. Small, S. Chen, J. Subbiah, C. M. Amb, S.-W. Tsang, T.-H. Lai, J. R. Reynolds, F. So, *Nat. Photonics* **2011**, *6*, 115.

[40] S. Shao, K. Zheng, T. Pullerits, F. Zhang, *ACS Appl. Mater. Interfaces* **2013**, *5*, 380.

[41] B. Yang, S. Zhang, S. Li, H. Yao, W. Li, J. Hou, *Adv. Mater.* **2019**, *31*, e1804657.

[42] H. C. Chen, S. W. Lin, J. M. Jiang, Y. W. Su, K. H. Wei, *ACS Appl. Mater. Interfaces* **2015**, *7*, 6273.

[43] F. Qin, L. Sun, H. Chen, Y. Liu, X. Lu, W. Wang, T. Liu, X. Dong, P. Jiang, Y. Jiang, L. Wang, Y. Zhou, *Adv. Mater.* **2021**, *33*, e2103017.

[44] X. Zheng, L. Zuo, F. Zhao, Y. Li, T. Chen, S. Shan, K. Yan, Y. Pan, B. Xu, C. Z. Li, M. Shi, J. Hou, H. Chen, *Adv. Mater.* **2022**, *34*, e2200044.

[45] G. Zeng, W. Chen, X. Chen, Y. Hu, Y. Chen, B. Zhang, H. Chen, W. Sun, Y. Shen, Y. Li, F. Yan, Y. Li, *J. Am. Chem. Soc.* **2022**, *144*, 8658.

[46] X. Liu, Z. Zheng, J. Wang, Y. Wang, B. Xu, S. Zhang, J. Hou, *Adv. Mater.* **2022**, *34*, e2106453.

[47] Y. Han, Z. Hu, W. Zha, X. Chen, L. Yin, J. Guo, Z. Li, Q. Luo, W. Su, C. Q. Ma, *Adv. Mater.* **2022**, *34*, e2110276.

[48] W. Pan, Y. Han, Z. Wang, C. Gong, J. Guo, J. Lin, Q. Luo, S. Yang, C.-Q. Ma, *J. Mater. Chem. A* **2021**, *9*, 16889.

[49] Y. Han, X. Chen, J. Wei, G. Ji, C. Wang, W. Zhao, J. Lai, W. Zha, Z. Li, L. Yan, H. Gu, Q. Luo, Q. Chen, L. Chen, J. Hou, W. Su, C. Q. Ma, *Adv. Sci.* **2019**, *6*, 1901490.

[50] J. Zhang, Y. Zhao, J. Fang, L. Yuan, B. Xia, G. Wang, Z. Wang, Y. Zhang, W. Ma, W. Yan, W. Su, Z. Wei, *Small* **2017**, *13*, 1700388.

[51] L. Mao, Q. Chen, Y. Li, Y. Li, J. Cai, W. Su, S. Bai, Y. Jin, C.-Q. Ma, Z. Cui, L. Chen, *Nano Energy* **2014**, *10*, 259.

[52] F. C. Krebs, S. A. Gevorgyan, J. Alstrup, *J. Mater. Chem.* **2009**, *19*, 5442.

[53] G. P. Kushto, W. Kim, Z. H. Kafafi, *Appl. Phys. Lett.* **2005**, *86*, 093502.

[54] W. J. Beek, M. M. Wienk, M. Kemerink, X. Yang, R. A. Janssen, *J. Phys. Chem. B* **2005**, *109*, 9505.